GASP XXXVIII: the LOFAR-MeerKAT-VLA view on the nonthermal side of a jellyfish galaxy

Ignesti, A.; Vulcani, B.; Poggianti, B.M.; Paladino, R.; Shimwell, T.; Healy, J.; ... ; Verheijen, M.

The Astrophysical Journal, 924:64 (15pp), 2022 January 10 https://doi.org/10.3847/1538-4357/ac32ce

GASP XXXVIII: The LOFAR-MeerKAT-VLA View on the Nonthermal Side of a Jellyfish Galaxy

Alessandro Ignesti[1], Benedetta Vulcani[1], Bianca M. Poggianti[1], Rosita Paladino[2], Timothy Shimwell[3,4], Julia Healy[3,5,6], Myriam Gitti[2,7], Cecilia Bacchini[1], Alessia Moretti[1], Mario Radovich[1], Reinout J. van Weeren[4], Ian D. Roberts[4], Andrea Botteon[4], Ancla Müller[8], Sean McGee[9], Jacopo Fritz[10], Neven Tomičić[1], Ariel Werle[1], Matilde Mingozzi[11], Marco Gullieuszik[1], and Marc Verheijen[5]

[1] Istituto Nazionale di Astrofisica-Padova Astronomical Observatory, Vicolo dell'Osservatorio 5, I-35122 Padova, Italy; alessandro.ignesti@inaf.it
[2] Istituto Nazionale di Astrofisica, Istituto di Radioastronomia di Bologna, via Piero Gobetti 101, I-40129 Bologna, Italy
[3] ASTRON, the Netherlands Institute for Radio Astronomy, Postbus 2, 7990 AA Dwingeloo, The Netherlands
[4] Leiden Observatory, Leiden University, P.O. Box 9513, 2300 RA Leiden, The Netherlands
[5] Kapteyn Astronomical Institute, University of Groningen, Landleven 12, 9747 AV Groningen, The Netherlands
[6] Department of Astronomy, University of Cape Town, Private Bag X3, Rondebosch 7701, South Africa
[7] Dipartimento di Fisica e Astronomia, Universitá di Bologna, via Piero Gobetti 93/2, I-40129 Bologna, Italy
[8] Ruhr University Bochum, Faculty of Physics and Astronomy, Astronomical Institute, Universitätsst 150, D-44801 Bochum, Germany
[9] School of Physics and Astronomy, University of Birmingham, Birmingham B15 2TT, UK
[10] Instituto de Radioastronomía y Astrofísica, UNAM, Campus Morelia, A.P. 3-72, C.P. 58089, Mexico
[11] Space Telescope Science Institute, 3700 San Martin Drive, Baltimore, MD 21218, USA
Received 2021 August 6; revised 2021 October 22; accepted 2021 October 23; published 2022 January 12

Abstract

Ram pressure stripping is a crucial evolutionary driver for cluster galaxies. It is thought to be able to accelerate the evolution of their star formation, trigger the activity of their central active galactic nucleus (AGN) and the interplay between galactic and environmental gas, and eventually dissipate their gas reservoirs. We explored the outcomes of ram pressure stripping by studying the nonthermal radio emission of the jellyfish galaxy JW100 in the cluster A2626 ($z = 0.055$), by combining LOw Frequency Array, MeerKAT, and Very Large Array observations from 0.144 to 5.5 GHz. We studied the integrated spectra of the stellar disk, the stripped tail, and the AGN; mapped the spectral index over the galaxy; and constrained the magnetic field intensity to between 11 and 18 μG in the disk and <10 μG in the tail. The stellar disk radio emission is dominated by a radiatively old plasma, likely related to an older phase of a high star formation rate. This suggests that the star formation was quickly quenched by a factor of 4 in a few 10^7 yr. The radio emission in the tail is consistent with the stripping scenario, where the radio plasma that originally accelerated in the disk is subsequently displaced in the tail. The morphology of the radio and X-ray emissions supports the scenario of the accretion of magnetized environmental plasma onto the galaxy. The AGN nonthermal spectrum indicates that relativistic electron acceleration may have occurred simultaneously with a central ionized gas outflow, thus suggesting a physical connection between the two processes.

Unified Astronomy Thesaurus concepts: Radio astronomy (1338); Galaxies (573)

1. Introduction`

Spiral galaxies residing in clusters are commonly observed as being redder and having less star formation than field galaxies of similar mass (e.g., Kennicutt 1989; Gavazzi et al. 2006), thus indicating that the cluster environment could play the role of "accelerator" in galaxy evolution (e.g., Guglielmo et al. 2015). Environmental processing could either be due to gravitational interactions, in the form of tidal interplay with both the cluster and the other galaxies, or hydrodynamical interactions with the environmental plasma (e.g., van Gorkom 2004; Boselli & Gavazzi 2006). The latter, being able to completely remove the gas contents of the galaxies, can dramatically impact their morphology and evolution (e.g., Boselli et al. 2021, for a review). As galaxies orbit through the cluster, the intracluster medium (ICM) exerts a pressure, known as ram pressure stripping (RPS), on the galactic medium. Such pressure scales as $\rho_{\rm ICM}v^2$ (e.g., Gunn & Gott 1972), where $\rho_{\rm ICM}$ is the mass density of the ICM (typically 10^{-27}–10^{-28} g cm^{-3}; e.g., Sarazin 1986) and v is the galaxy velocity relative to the ICM (∼500–1000 km s^{-1}; e.g., Cava et al. 2009). This external pressure can directly strip the interstellar medium (ISM) out of the disk, leaving a wake of material trailing the galaxy. The gas loss induced by this process can lead to rapid decreases in the star formation rate (SFR) in these galaxies. The most extreme examples of galaxies undergoing strong ram pressure are the so-called jellyfish galaxies (e.g., Smith et al. 2010; Ebeling et al. 2014; Fumagalli et al. 2014; Poggianti et al. 2017b). These objects show one-sided extraplanar debris visible in the optical/UV light, and striking tails of ionized gas. Jellyfish galaxies represent a transitional phase between infalling star-forming spirals and quenched cluster early-type galaxies, and they provide a unique opportunity to understand the impacts of gas removal processes on galaxy evolution. Interestingly, RPS can also trigger a plethora of (poorly understood) phenomena, such as the formation of cold extraplanar gas, which leads to the formation of new stars outside the disk (e.g., Poggianti et al. 2019a; Gullieuszik et al. 2020); the activity of the central active galactic nucleus (AGN; e.g., Poggianti et al. 2017a; Peluso et al. 2021), or complex mixing between the ICM and ISM (e.g., Sun et al. 2010; Poggianti et al. 2019b; Campitiello et al. 2021).

The radio continuum emission can be a powerful probe for investigating these phenomena. From the radio point of view, cluster late-type galaxies are generally characterized by an excess of radio emission, which has been interpreted as possible evidence of star formation enhancement due to RPS (e.g., Gavazzi & Boselli 1999; Murphy et al. 2009; Vollmer et al. 2013; Chen et al. 2020; Roberts et al. 2021b). In general, the radio continuum emission in spiral galaxies is composed of the thermal emission of the $\sim 10^4$ K plasma in the H II regions and the nonthermal synchrotron emission of the relativistic cosmic ray electrons (CRe), which are accelerated by supernovae (SNe) shocks (e.g., Condon 1992, for a review) and reach energies of few GeV. The nonthermal emission provides us with a wealth of information. Given that it is directly related to SNe, and due to the fact that galaxies are generally optically thin at GHz frequencies, the nonthermal continuum is a reliable proxy of the SFR (e.g., Bell et al. 2003; Murphy et al. 2011; Tabatabaei et al. 2017; Gürkan et al. 2018). Moreover, the ISM microphysics, as well as the magnetic field, can be probed by studying the CRe properties traced by their nonthermal emission (e.g., Vollmer et al. 2009, 2013; Basu et al. 2015; Heesen et al. 2016, 2019; Klein et al. 2018). The study of the radio emission in jellyfish galaxies has recently allowed a series of important advances. The study presented in Müller et al. (2021) explored the magnetic field in the tail of jellyfish galaxy JO206, finding for the first time evidence of an ordered, large-scale field likely induced by the accretion of an envelope of magnetized ICM (this process is also known as magnetic draping; see Dursi & Pfrommer (2008), Pfrommer & Dursi (2010), and Sparre et al. (2020) for further details). Moreover, new surveys of radio jellyfish galaxies, made possible by the advent of new generation radio observatories, such as the LOw Frequency Array (LOFAR), have discovered new populations of galaxies with extended, asymmetrical radio emission both in clusters and groups (Roberts et al. 2021a, 2021b).

In this work, we explore—for the first time—the nonthermal, multifrequency radio emission of the jellyfish galaxy JW100 ($z = 0.062$; also known as IC 5337) in the galaxy cluster A2626 ($z = 0.055$), which is a spectacular playground for studying the outcomes of RPS. Selected by Poggianti et al. (2016) as a stripping candidate, it is one of the jellyfish galaxies in the GAs Stripping Phenomena (GASP;[12] Poggianti et al. 2017b) sample. JW100 is characterized by one of the most striking ionized gas tails in the sample (Figure 1), and it is also the most massive galaxy in GASP, with a stellar mass of $30 \times 10^{10}\ M_\odot$ and a total SFR of $4.0 \pm 0.8 M_\odot\ \mathrm{yr}^{-1}$, of which $2.6 \pm 0.5 M_\odot\ \mathrm{yr}^{-1}$ is in the tail (Vulcani et al. 2018). Its stellar mass and SFR place JW100 about 0.4 dex below the SFR–mass relation for normal galaxies, and ~0.65 dex below the relation for jellyfish galaxies (Vulcani et al. 2018), indicating that star formation has already decreased due to gas-stripping. The effects of RPS in JW100 extend beyond the SFR quenching: in addition to the possible connection between RPS and AGN activity explored in Poggianti et al. (2017a), Moretti et al. (2018, 2020a) reported the discovery of molecular gas clouds in the tail, whose locations are inconsistent with a scenario of stripping from the disk, thus suggesting that they were formed in situ as a possible consequence of a fast conversion of H I into H_2 (see Moretti et al. (2020b) for further details). Finally, by exploring the spatial correlation between the Hα and X-ray emission in the tail of JW100, and by studying the spectral properties of the latter, Poggianti et al. (2019b) suggested that the Hα emission in the stripped tail (whose optical spectral properties cannot be explained by star formation only; see Poggianti et al. (2019a)) could be the result of the complex interplay between ISM and ICM, triggered by RPS.

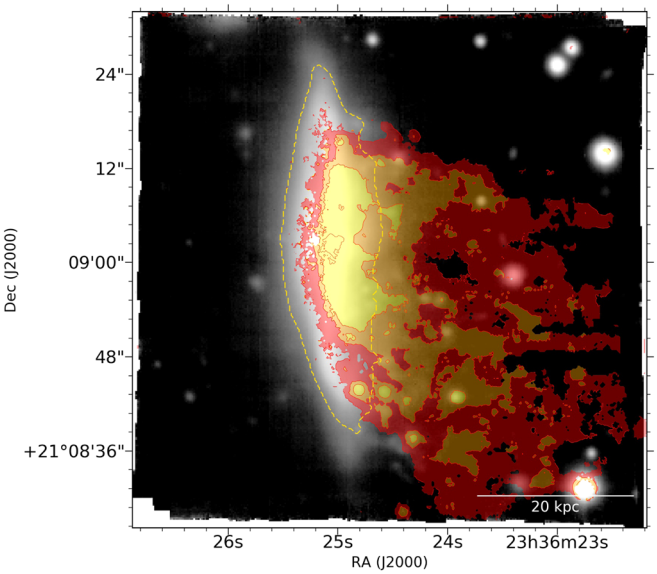

Figure 1. MUSE white light image of JW100, overlaid with the contours of the Hα emission (the filled area) and the stellar continuum (the gold dashed line), as defined in Gullieuszik et al. (2020).

Previous preliminary studies of the radio continuum of JW100 that focused on the 0.144 and 1.4 GHz emission, were presented in Ignesti et al. (2020) and Poggianti et al. (2019a), respectively. Here, we combine multiple radio observations in an unprecedented multifrequency study that aims to probe the origin and properties of the CRe, and, by doing so, further explore the history of this galaxy. This paper is structured as follows. In Section 2, we present the data sets and the new images produced for this analysis. In Section 3, the properties of the nonthermal emission inferred from these images are reported, while in Section 4 our findings are discussed and interpreted in the context of the galaxy's evolution.

In this paper, we use a Chabrier (2003) initial mass function (IMF) and the standard concordance cosmology parameters $H_0 = 70\ \mathrm{km\ s^{-1}\ Mpc^{-1}}$, $\Omega_M = 0.3$, and $\Omega_\Lambda = 0.7$. At the redshift of A2626 ($z = 0.055$; Cava et al. 2009), this yields $1'' = 1.071$ kpc.

2. Data Analysis

In this study, we present a multifrequency continuum analysis that combines radio observations at 0.144, 1.4, 3.2, and 5.5 GHz obtained with the LOFAR, MeerKAT, and Karl G. Jansky Very Large Array (VLA) radio telescopes, respectively. The data involved in this work have already been published in the literature. We present below a brief description of the processing of each data set, with the corresponding references, in which further details are provided.

In order to probe the low-frequency emission at 0.144 GHz, we made use of the LOFAR observation of A2626 presented in Ignesti et al. (2020), which is part of the P353+21 pointing of the LOFAR Two-meter Sky Survey (LoTSS)

[12] http://web.oapd.inaf.it/gasp/index.html

(Shimwell et al. 2017, 2019). The data set was processed using the data reduction pipeline DDF-PIPELINE v. 2.2 developed by the LOFAR Surveys Key Science Project,[13] and an additional self-calibration was applied to a smaller region (∼1 deg) centered on the central galaxy IC5338, following the procedure presented in van Weeren et al. (2021). The 1.4 GHz emission was explored by means of a recent MeerKAT observation of the cluster presented in Healy et al. (2021) (project SCI-20190418-JH-01). The data set was divided in two bands (0.960–1.16 and 1.300–1.520 GHz) and processed by following the general strategy presented in Serra et al. (2019) for cross-calibration using CARAcal (Józsa et al. 2020).[14] Here we present the analysis of the 1.300–1.520 GHz band.

Finally, we probed the high-frequency emission by exploiting the VLA observations of the cluster at 3.0 and 5.5 GHz obtained in the C-configuration (project code: 14B-022; PI: Gitti) that are presented in Ignesti et al. (2017). The data reduction was done using the National Radio Astronomy Observatory Common Astronomy Software Applications package (CASA; McMullin et al. 2007), version 4.6. Due to the flagging of radio frequency interference, the bandwidth of the 3 GHz observation decreased from 2.0 GHz (2.0–4.0 GHz) to 1.6 GHz (2.4–4.0 GHz), thus moving the central frequency from 3.0 to 3.2 GHz.

We produced new images of JW100 at different frequencies using WSCLEAN v2.10.1 (Offringa et al. 2014). We tested different combinations of Briggs weightings (Briggs 1995), with `robust` values ranging from 0 to −2 and multi-scale cleaning (Offringa & Smirnov 2017). For the LOFAR data, we adopted a lower UV cut of 80 λ, corresponding to an angular scale of 43′, to drop the shortest spacings where calibration is more challenging (see Shimwell et al. (2017) for further details about the imaging of LoTSS observations). The final images are presented in Figure 2, while in Table 1 we report the corresponding resolution and root mean square (rms) noise. The latter was measured for each map by using the same set of rectangular boxes manually placed on regions of the sky within 15′ of JW100, and devoid of other radio sources. Moreover, in order to reliably compare the flux densities at the different frequencies, we produced a second set of images with matched UV ranges (670–19000 λ) and resolutions (12″ × 12″), which we report in Figure 3. In order to reliably compare the signal collected by the different UV-sampling configurations, we adopted an `UNIFORM` weighting for the MeerKAT and VLA data. For the LOFAR data, a different weighting was adopted (`ROBUST = −1`), to detect the extended emission that was lost using the UNIFORM weight (see the bottom-left panel of Figure 1 in Ignesti et al. (2020)). For consistency, the rms levels of these images (Table 1) were evaluated by using the same set of regions adopted for the high-resolution images.

We jointly analyzed the radio emission of JW100 with a Multi Unit Spectroscopic Explorer (MUSE) optical observation in order to carry out a multiwavelength analysis of the galaxy. The MUSE observations, the data reduction, and the methods of analysis are described in Poggianti et al. (2017b). Specifically, we analyzed the nebular Balmer emission line of Hα, which is measured from the MUSE datacube with both the optically thin corrections for the galactic foreground dust extinction as well as the intrinsic dust extinction and stellar absorption. Finally, we also included the high-resolution VLA observation at 1.4 GHz presented in Gitti (2013) (1.″3), to study the morphology of the AGN radio emission, and the Chandra X-ray observation of A2626 (Ignesti et al. 2018), to evaluate the spatial correlation between the distributions of the relativistic and hot plasmas.

[13] https://github.com/mhardcastle/ddf-pipeline
[14] https://github.com/caracal-pipeline/caracal

3. Results

3.1. Radio Continuum Images

The images reported in Figures 2 and 3 show that the morphology of the emission changes with frequency. The radio emission extends from the stellar disk toward the southwest, roughly following the morphology of the Hα emission (Figure 1). At the current resolution and sensitivity, the projected length of the extraplanar radio emission, i.e., the radio tail (here defined as the extension of the radio emission from the edge of the stellar disk to the farthest 3× rms level contour outside the disk, along the direction of the Hα tail, as measured in the high-resolution images and not deconvolved for the beam smearing), decreases from ∼37 kpc at 144 MHz to almost zero at 5.5 GHz. While the disk emission is clearly distorted at 3.2 and 5.5 GHz, the tail is too faint to be confirmed at these frequencies. Indeed by assuming a spectral index of $\alpha = -0.7$, and given the current rms levels at 1.4, 3.2, and 5.5 GHz (Table 1), the 3× rms level contours of the 0.144 GHz image would correspond to detection levels of 3.5×, 2.4×, and 1.3× rms, respectively. The absence of the clear detection of the tail at 3.2 and 5.5 GHz is therefore not a surprise.

Within the stellar disk, the continuum emission is more extended in the north–south direction at 1.4 and 3.2 GHz than at 0.144 and 5.5 GHz. In contrast, two features—i.e., the presence of the AGN radio emission at the center, and the symmetrically truncated emission with respect to the stellar disk—can be observed at every frequency. Examples of radio disk truncation have already been reported in the literature (e.g., Vollmer et al. 2009, 2013; Chen et al. 2020; Roberts et al. 2021b), and they have been claimed to be a result of ram pressure stripping. The implications of the morphology of the radio emission are discussed in Section 4.2.

Finally, we note that the radio emission in the top-left corners of the LOFAR and MeerKAT images is part of the Kite radio source located at the center of A2626 (Ignesti et al. 2020, and references therein). Although we do not observe significant negative artifacts around the galaxy in the 0.144 GHz image (which indicates that the cleaning of the brighter Kite source did not dramatically affect the morphology of JW100), the resolution of our image merges the two sources, to the east of the galaxy and the northern part of the tail. As we discuss in the following section, we carefully accounted for this during our study of the radio tail.

3.2. Resolved Radio Properties

The resolution reached in these observations allows us to explore the properties of the radio emission in three different regions: the AGN, the stellar disk, and the stripped tail. These regions, which are reported in Figure 4, are defined as follows:

1. AGN: we defined a 12″ (∼12 × 12 kpc) diameter circular region, centered on the surface brightness peak observed at 0.144 MHz, that coincides with the point

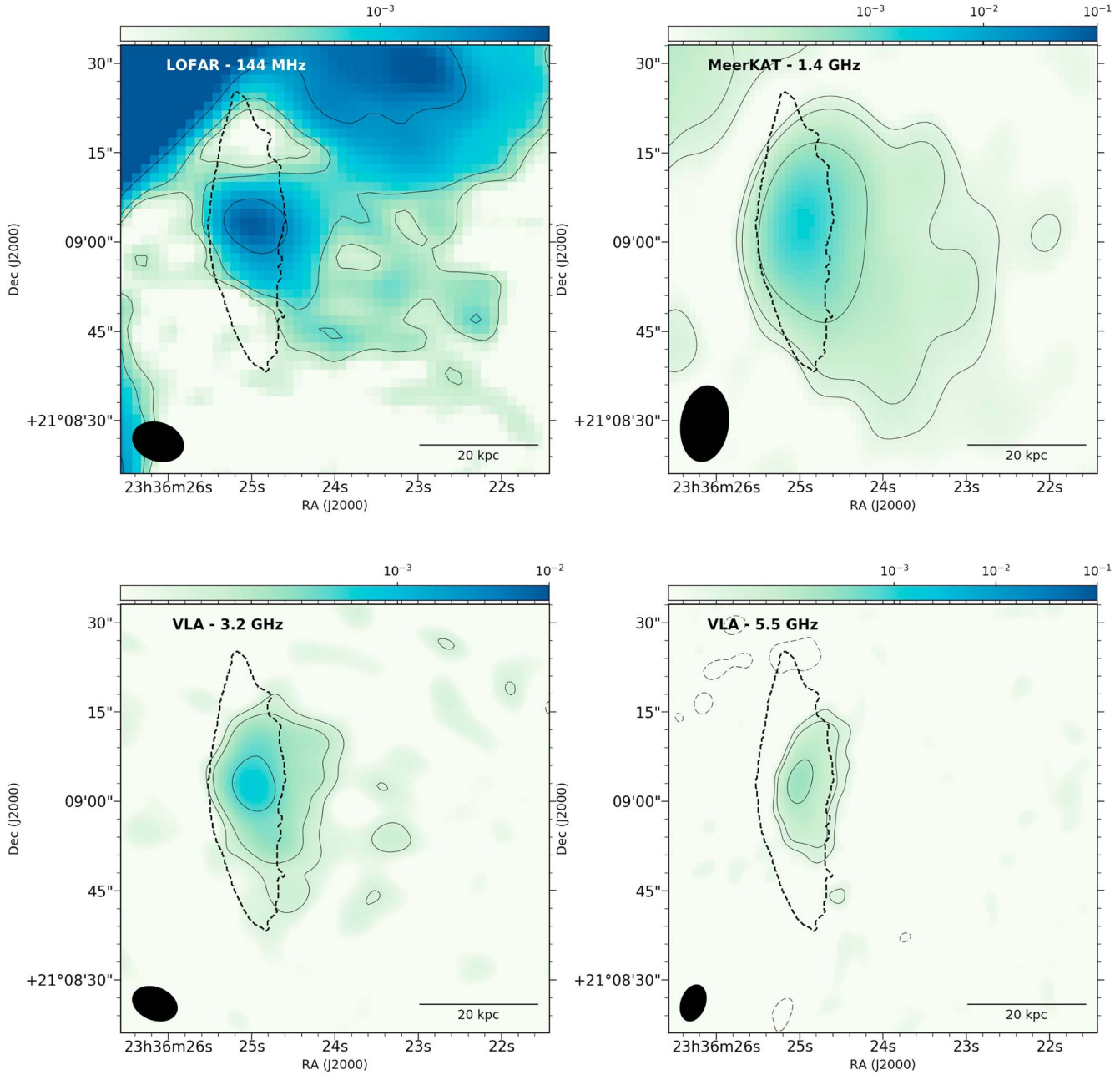

Figure 2. Images of JW100 at different frequencies, with the overlaid contours corresponding to the −3, 3, 6, 12, and 24× rms levels (the continuous lines) and the stellar continuum emission (the dashed lines). The respective rms and resolution (shown by the black filled ellipses in the bottom-left corner of each image) at each frequency are reported in Table 1.

Table 1
Properties of the Radio Images Reported in Figures 2 and 3

Frequency (GHz)	Resolution (arcsec)	Rms (1) (μJy beam^{-1})	Rms (2) (μJy beam^{-1})
0.144	8.8 × 6.4	93.8	142.2
1.4	12.4 × 7.7	16.2	24.4
3.2	7.8 × 5.4	15.0	20.4
5.5	6.3 × 4.1	6.0	25.4

Note. (1) and (2) indicate the rms measured before and after the smoothing to the 12″ × 12″ resolution.

source studied in Poggianti et al. (2017a, 2019b) and Radovich et al. (2019). Its properties are discussed in Section 4.3.

2. Stellar disk: Gullieuszik et al. (2020) defined the stellar disk of JW100 on the basis of the Hα emission observed with MUSE. Due to the difference in resolution between the optical and radio images, we had to define the size of the stellar disk accordingly. We produced a smoothed Hα image to match the resolution of the smoothed radio images, then we estimated the size of the smoothed stellar disk by defining an ellipse containing the same Hα flux as measured within the stellar disk in the original image. For each radio map, this allowed us to define the disk emission as the radio flux density above the 3× rms level measured within the elliptical region shown in Figure 4. For the 0.144 GHz image, we did not include the emission of the Kite present in the northern part of the elliptical region.

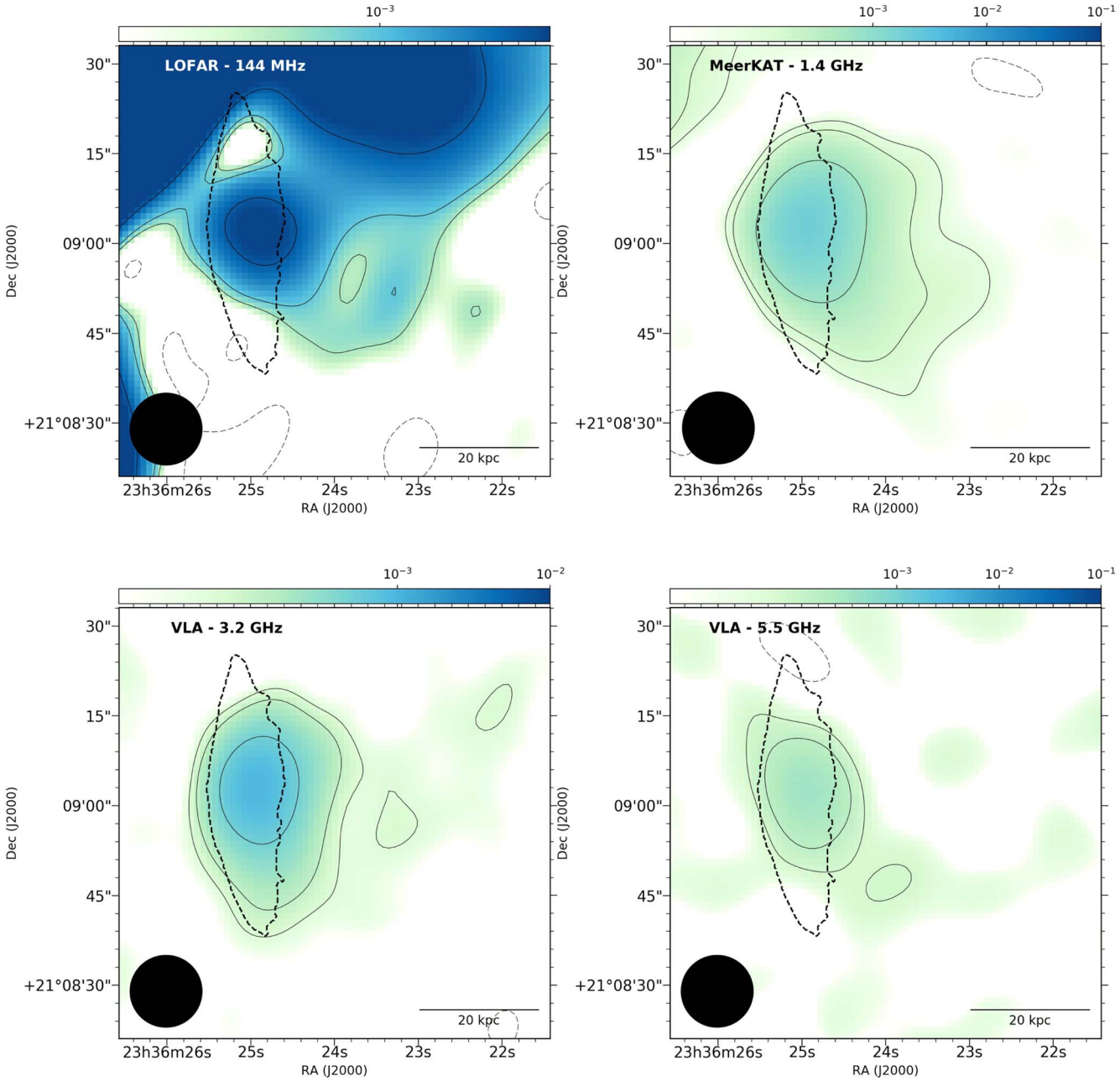

Figure 3. Images of JW100 at different frequencies, smoothed with a $12'' \times 12''$ Gaussian beam, which is shown in the bottom-left corners of the images. We also report, on top, the contours corresponding to the -3, 3, 6, 12, and $24\times$ rms levels (the continuous lines) and the stellar continuum emission (the dashed lines). The respective rms at each frequency are reported in Table 1.

3. Tail: we defined a region along the Hα tail that was long enough to minimize the possible contributions from the disk and, at 0.144 GHz, the northern plume of the Kite radio source. At 0.144 and 1.4 GHz, we clearly resolved the extended radio emission within this region, while at 3.2 GHz we only had a tentative detection, thus we estimated a reference value for the flux density by multiplying the $3\times$ rms level for the area of tail region. This provided us with a generous upper limit for prudently constraining the nonthermal spectrum up to 3.2 GHz. At 5.5 GHz, in the low-resolution image only, we observed a component of an emission in this region, with an angular size below the resolution of the map. Due to the fact that it does not spatially coincide with the emission observed at 3.2 GHz, we could not exclude the possibility that it is an artifact, and hence we conservatively decided to restrict the analysis of the stripped tail to the 0.144–3.2 GHz band.

These regions were used to measure the radio flux densities in the smoothed radio images (Figure 3). We assumed calibration errors of 20%, 10%, 5%, and 5% for the emission at 0.144, 1.4, 3.2, and 5.5 GHz, respectively. We computed the net flux density in the disk by subtracting, at each frequency, the AGN contribution from the total emission. In the following, therefore, we refer to "disk emission" as the net radio emission within the stellar disk devoid of the AGN contribution.

As mentioned in Section 1, the total radio emission is the result of the combination of the nonthermal CRe synchrotron

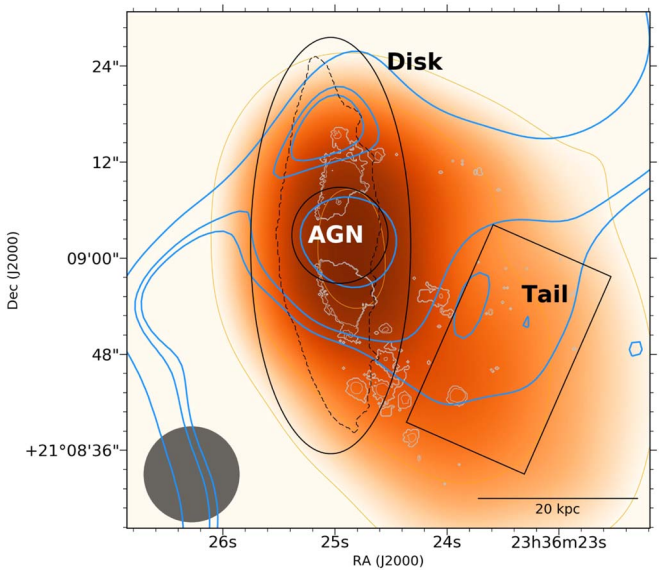

Figure 4. MUSE Hα emission (Figure 1) smoothed to 12″ (the color image and orange contours), with the contours of the stellar continuum (the black dashed line), the spaxels classified as star-forming (the silver contours; see Poggianti et al. 2019a), and the regions (the geometrical shapes marked by the solid black lines). For reference, we also report the positive contours of the 0.144 GHz image shown in Figure 3 (blue) and the beam shape (the solid black circle in the bottom-left corner).

emission and the thermal radio emission provided by the warm ISM. Therefore, to estimate the nonthermal emission, $S_{\rm nt}$, we have to subtract the optically thin thermal component, $S_{\rm th}$, from the total measured flux densities, $S_{\rm tot}$: $S_{\rm nt} = S_{\rm tot} - S_{\rm th}$. The thermal flux, $S_{\rm th}$, can be expressed as:

$$S_{\rm th} = 1.14 \times 10^{-14} \left(\frac{T_e}{10^4\ {\rm K}}\right)^{0.34} \left(\frac{\nu}{\rm GHz}\right)^{-0.1} S_{\rm H\alpha}, \qquad (1)$$

where $S_{\rm H\alpha}$ is the Hα flux measured in the smoothed Hα image (Figure 4) in units of erg s^{-1} cm^{-2}, and T_e is the thermal electron temperature, which we assume to be 10^4 K (e.g., Deeg et al. 1997; Tabatabaei et al. 2017). We note that, due to the complex interplay between ISM and ICM that is taking place in this galaxy, the ionized ISM could potentially reach temperatures up 10^6 K (e.g., Kanjilal et al. 2020), hence the thermal radio emission might be more relevant. The current data does not allow us to reliably determine the temperature of the ionized ISM, hence we cannot exclude the possibility that we may be underestimating the contribution of the thermal radio emission, especially in the tail, where the ISM–ICM interplay is potentially more significant (see Poggianti et al. 2019b).

In Figure 5 and Table 2, we report the resulting nonthermal flux densities, the fractions of the thermal radio flux with respect to the total ($f_{\rm th} = S_{\rm th}/S_{\rm tot}$), and the nonthermal spectral index in the three bands (0.144–1.4, 1.4–3.2, and 3.2–5.5 GHz) computed as:

$$\alpha_{\nu_1}^{\nu_2} = \frac{\log\left(\frac{S_1}{S_2}\right)}{\log\left(\frac{\nu_1}{\nu_2}\right)} \pm \frac{1}{\log\left(\frac{\nu_1}{\nu_2}\right)} \sqrt{\left(\frac{\sigma_1}{S_1}\right)^2 + \left(\frac{\sigma_2}{S_2}\right)^2}, \qquad (2)$$

where ν, S, and σ are the frequency, the nonthermal flux density, and the corresponding error, respectively.

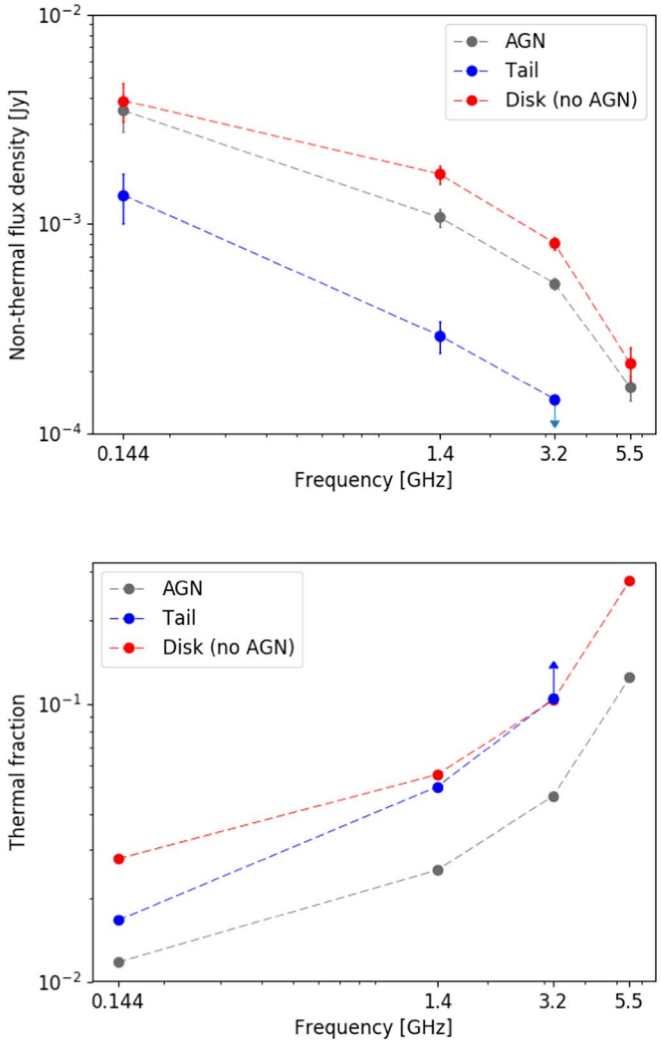

Figure 5. Nonthermal spectra (top) and thermal fractions (bottom) for the AGN, disk, and stripped tail. At 3.2 GHz, we report the upper limits of the stripped tail nonthermal flux density and thermal fraction.

The nonthermal integrated spectra of the three components present a series of interesting features:

1. The AGN spectrum steepens from $\alpha = -0.52 \pm 0.10$ at low frequencies to $\alpha = -2.10 \pm 0.28$ at 5.5 GHz. As a caveat, we note that the combination of the low angular resolution and the edge-on view of the disk does not allow us to completely rule out contamination from the disk emission. We discuss the AGN nonthermal spectrum in the context of the previous studies in Section 4.3.
2. The synchrotron emission in the disk shows both an evident flattening at low frequencies ($\alpha = -0.35 \pm 0.10$) and a strong steepening at higher frequencies. The low-frequency flattening is expected, as a consequence of the ionization losses of low-energy CRe in the high-density, star-forming regions (e.g., Murphy 2009; Basu et al. 2015; Chyży et al. 2018). The steepening at high frequencies indicates that the relativistic plasma is old enough to have been affected by significant energy losses (e.g., Pacholczyk 1970; Klein et al. 2018). Interestingly, Vulcani et al. (2018) and Poggianti et al. (2019a) report on the ongoing star formation within the disk, which would entail the injection of fresh relativistic plasma

Table 2
Results of the Resolved Analysis

Nonthermal Flux Density S_{nt} [mJy]				
Region	0.144 GHz	1.4 GHz	3.2 GHz	5.5 GHz
AGN	3.48 ± 0.71	1.00 ± 0.11	0.52 ± 0.03	0.17 ± 0.02
Disk	3.88 ± 0.81	1.73 ± 0.18	0.81 ± 0.06	0.22 ± 0.04
Tail	1.37 ± 0.37	0.29 ± 0.05	<0.15	#
Thermal fraction f_{th}				
Region	0.144 GHz	1.4 GHz	3.2 GHz	5.5 GHz
AGN	0.01	0.03	0.05	0.12
Disk	0.03	0.06	0.10	0.28
Tail	0.02	0.05	>0.10	#
Nonthermal spectral index $\alpha_{\nu_1}^{\nu_2}$				
Region	0.144–1.4		1.4–3.2	3.2–5.5
AGN	-0.52 ± 0.10		-0.88 ± 0.14	-2.10 ± 0.28
Disk	-0.35 ± 0.10		-0.92 ± 0.15	-2.43 ± 0.37
Tail	-0.68 ± 0.14		<-0.85	#

Note. For each region, we report the nonthermal radio flux densities (mJy; top), the thermal fraction (middle), and the nonthermal spectral indexes (bottom). Those values are not reported for the tail at 5.5 GHz, due to the concerns regarding the reliability of the detection.

emitting with a spectral index of $-0.7 < \alpha < -0.5$ up to 5.5 GHz. Therefore, the steep integrated spectrum suggests an inhomogeneity in the CRe distribution, meaning that the steep-spectrum emission results from the mixing of old and fresh CRe within the disk (e.g., Chyży et al. 2018; Heesen et al. 2019). The connection between nonthermal radio emission and the SFR is further discussed in Section 4.1;

3. The spectrum of the tail is steeper than the disk in the 0.144–1.4 GHz band (-0.68 ± 0.14 versus -0.35 ± 0.10), and potentially also in the 1.4–3.2 GHz band (<-0.85 and -0.92 ± 0.15). This is in agreement with what is reported in Müller et al. (2021) for the jellyfish galaxy JO206.

Finally, the thermal fractions increase with frequency, in agreement with the results reported in the literature (e.g., Tabatabaei et al. 2017).

3.3. Spectral Index Maps

We combined the smoothed images at 0.144, 1.4, and 3.2 GHz (Figure 3) in order to map the spectral indexes of the total radio emission from disk to tail in the 0.144–1.4 and 1.4–3.2 GHz bands. We excluded the 5.5 GHz map from this analysis because it does not provide significant information about the extended emission. For each map, we selected the emission above the respective $3\times$ rms levels, and we computed the spectral indexes pixel-by-pixel, following Equation (2). The thermal fractions reported in Figure 5 show that the thermal contribution below 3.2 GHz is negligible, thus the resulting values well represent the nonthermal component. The resulting images and the corresponding error maps are presented in Figure 6.

As seen from the flux density measurements, the spectral index maps show a generally flat spectrum in the disk ($\alpha > -0.7$), and a steepening toward the tail ($\alpha < -0.8$). In the 0.144–1.4 GHz maps, we observe that the flat-spectrum regions roughly coincide with the star-forming regions selected according to the [O I] Baldwin, Phillips & Telervich (BPT) diagrams reported in Poggianti et al. (2019a; see Figure 4),[15] both within and outside the stellar disk, suggesting that the CRe there are younger, i.e., freshly injected. The flattest spectrum regions ($\alpha \simeq -0.3 \mp 0.1$) are located at the disk edges, in agreement with the integrated spectrum (Table 2). The spectral steepening trend outside the disk resembles the previous results presented in the literature (e.g., Vollmer et al. 2004; Müller et al. 2021), and this can provide evidence that the plasma in the tail is generally older than that in the disk, i.e., that the CRe are accelerated in the disk and then stripped away along the tail. We note that the steepest spectrum ($\alpha \simeq -1.4$) is observed in the direction of the northern, ultra-steep spectrum plume of the Kite radio source (see Ignesti et al. 2020). On the basis of the striking difference in the spectral indexes between the galaxy and the plume (-1.4 versus <-3), we argue that the steepening is likely due to the combination of low resolution and projection effects that add the relatively flat spectrum tail to the ultra-steep emission of the Kite. The 1.4–3.2 GHz spectral map is generally more uniform, with values between -1.0 and -0.8. The southern edge of the disk exhibits a flat-spectrum edge ($\alpha \simeq -0.4 \pm 0.4$) that is barely in agreement with the integrated spectrum ($\alpha = -0.92 \pm 0.15$), thus we suggest that it may be an artifact produced by the similar rms levels of the two images.

3.4. Magnetic Field

Observing nonthermal radio emission implies that the galaxy is permeated by a magnetic field. Furthermore, the asymmetrical morphology suggest that the CRe within the tail are moving within a magnetic field that may either be extending from the disk or from the ICM magnetic field. The geometry and intensity of the magnetic field can determine the evolution of the stripped ISM (e.g., Gronke & Oh 2020; Sparre et al. 2020; Ge et al. 2021). However, inferring its intensity is not trivial. In the following, we present different estimates aimed at mapping the magnetic field strength in the galaxy.

To begin with, we evaluate the magnetic field at the stagnation point—i.e., the point in front of the galaxy, where the local wind velocity is zero—with respect to the ICM. The draping framework (Pfrommer & Dursi 2010; Sparre et al. 2020) predicts, in the case of a superAlfvénic motion (a condition that is always satisfied by a supersonic motion in a high-β plasma such as the ICM), the formation of a strong magnetic field in front of the galaxy, due to the accretion of a magnetic envelope composed of magnetized ICM. The magnetic field at the stagnation point would eventually reach a maximum value, B_{max}, of:

$$B_{max} = \sqrt{8\pi\tilde{\alpha}\rho V_p^2}, \quad (3)$$

where $\tilde{\alpha} = 2$ is a geometrical factor (see Dursi & Pfrommer (2008) for further details), ρ is the wind (i.e., the ICM) density, and V_p is the postshock velocity. In the JW100 condition in A2626, where the ICM density at the clustercentric projected radius is $\rho = 5.8 \times 10^{-27}$ g cm^{-3} (Ignesti et al. 2018),

[15] To be more conservative, we choose the [O I] over the [S II] diagram because it disentangles the star-forming regions in the tail from the rest of the Hα emission, whose origin is unclear (see Poggianti et al. (2019b) for a detailed discussion).

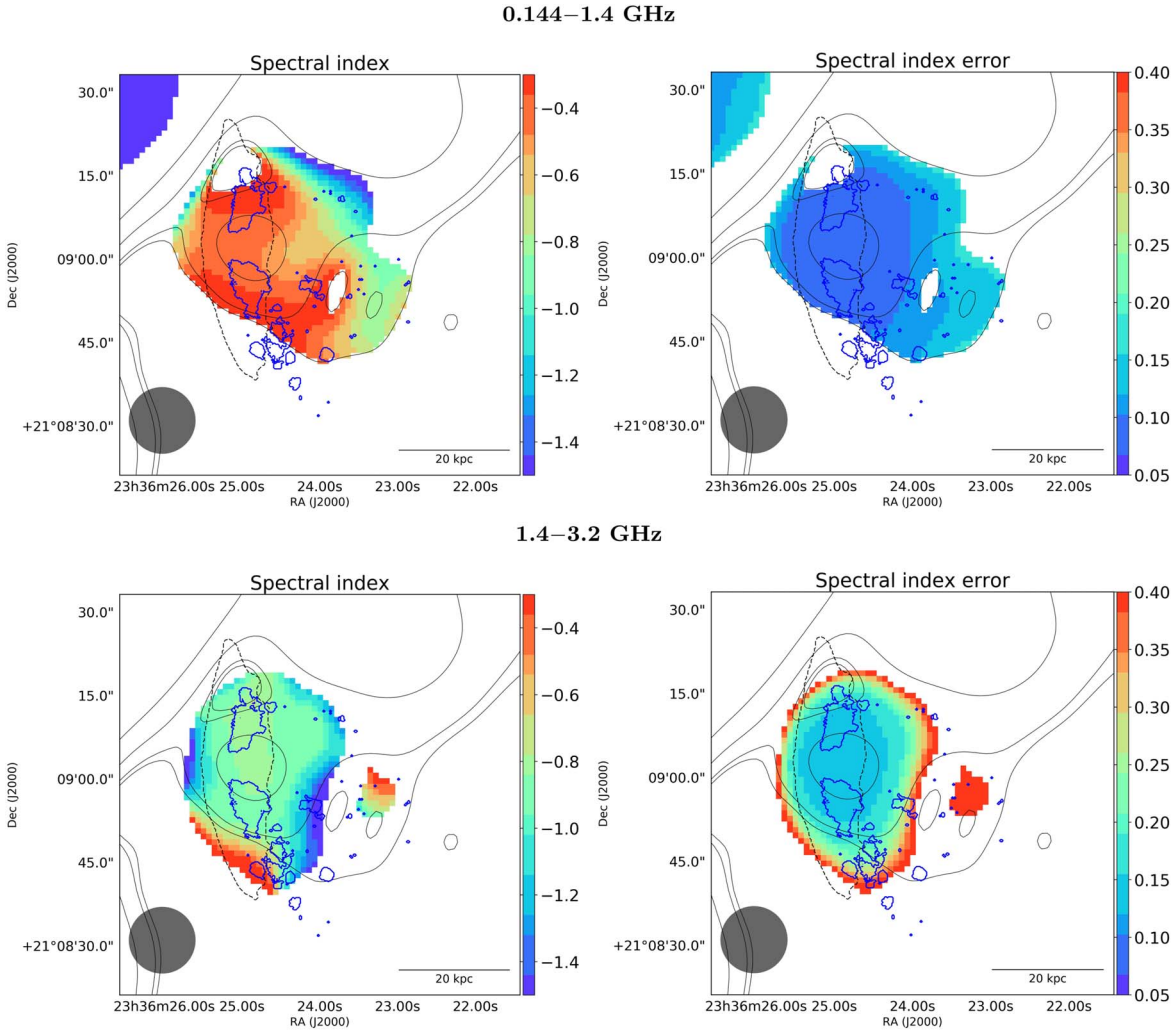

Figure 6. Spectral index (left) and error (right) maps for 0.144–1.4 GHz (top) and 1.4–3.2 GHz (bottom), with a resolution of $12'' \times 12''$ (the bottom-left corners). In each map, we also present the contours of the 144 MHz emission (the black continuous lines), the stellar continuum (the black dashed lines), and the contours of the star-forming regions reported in Figure 4 (the blue lines).

Equation (3) yields $B_{\rm max} \simeq 5 \times (V_p/100\ {\rm km\ s^{-1}})\ \mu$G. Therefore for V_p of the order of 2000 km s^{-1} (Poggianti et al. 2019b), the stagnation magnetic field could potentially reach extreme values ($\sim$100 μG). However, we note that such an estimate is based on the ICM density estimated at the projected clustercentric distance of JW100, thus it represents an upper limit for the actual ICM density surrounding JW100. The draping magnetic field should decline in intensity with the distance from the contact surface (Sparre et al. 2020), thus we could expect lower values in the disk and, even more so, in the tail.

We exploited two different methods in order to estimate the magnetic field within the disk.

1. We calculated the equipartition magnetic field following the revised formulation proposed in Beck & Krause (2005; Equation (3)). We used the nonthermal flux density measured at 1.4 GHz and corrected for redshift (see Govoni & Feretti 2004) to evaluate the synchrotron intensity. The spectral flattening at low frequencies did not permit us to reliably constrain the injection index, which is a direct proxy of the CRe energy distribution, thus we assumed a typical spectral index of $\alpha = -0.7$. The CRe pathlength was also unknown, thus we tested two extreme values of 1 and 2 kpc (Krause et al. 2018). Under these assumptions, the resulting equipartition field lies between 11 and 13 μG. As a caveat, we note that the equipartition estimate is based on the assumption of the equilibrium of the radio source. This hypothesis may not be true for the current state of JW100 because the external pressure provided by RPS could potentially affect the intensity of the magnetic field.
2. The theory of small-scale dynamo amplification predicts that the turbulence released by SNe (see, e.g., Bacchini et al. (2020) for a recent study) can locally amplify the magnetic field, thus inducing a connection between the latter and the SFR in the form of $B \propto {\rm SFR}^{0.3}$ (e.g., Gressel et al. 2008; Schleicher & Beck 2013). Tabatabaei et al. (2017) tested this hypothesis on the Key Insight in Nearby Galaxies Emitting in Radio (KINGFISHER) sample (Kennicutt et al. 2011), and provided an empirical relation:

$$\log(B) = (0.34 \pm 0.04)\log({\rm SFR}) + (1.11 \pm 0.02). \quad (4)$$

For JW100, Vulcani et al. (2018) report an SFR within the disk of 2.6 ± 0.5 that yields $B = 17.8 \pm 1.6$ μG. It is worth noticing that, for the current condition of JW100, other sources of turbulence related to RPS should be available, such as the propagation of the bow shock, which could further contribute to the magnetic field amplification (e.g., Iapichino & Brüggen 2012).

To summarize, these procedures constrain the average magnetic field between 11 and 18 μG within the disk, which is in agreement with the previous results for spiral galaxies (e.g., Beck 2000; Tabatabaei et al. 2017), but slightly higher than what is reported in Müller et al. (2021) for the jellyfish galaxy JO206 (6.5–7.8 μG). This could either be due to an intrinsic difference between the two galaxies (the stellar mass of JO206 is 9.1×10^{10} $M_{\odot}$, which is lower than that of JW100) or due to the uncertainties of the methods exploited for estimating the magnetic field.

The morphology of the tail and the local ISM properties are complex and mostly unknown, contrary to the situation with the disk, hence the methods described above cannot be reliably applied. Therefore, we estimated the magnetic field intensity by evaluating the cooling length. If the radio plasma is stripped from the disk, then the cooling length (i.e., the radio tail truncation scale) roughly corresponds to $D \simeq t_r \times v_{\rm pl}$, where $v_{\rm pl}$ is the velocity of the relativistic plasma and t_R is the radiative time of the CRe. Outside the stellar disk, the CRe cooling should mostly be dominated by synchrotron and Inverse Compton losses due to the cosmic microwave background (CMB). We assume that adiabatic losses are negligible because the stripped tails usually appear to be in quasi-equilibrium within the ICM (e.g., Sun et al. 2010; Zhang et al. 2013; Campitiello et al. 2021). Therefore, the radiative timescale, t_r, can be expressed as:

$$t_r \simeq 3.2 \times 10^{10} \frac{B^{1/2}}{B^2 + B_{\rm CMB}^2} \frac{1}{\sqrt{\nu(1+z)}} \ {\rm yr}, \quad (5)$$

where $B_{\rm CMB} = 3.25(1+z)^2$ μG is the equivalent CMB magnetic field and ν—in units of MHz—is the cut-off frequency (e.g., Miley 1980). Therefore, within this simple framework, the cooling length at a given frequency can be predicted based on the combination of the average magnetic field and the velocity of the CRe. Accordingly, the observed truncation scale can be used to jointly constrain these parameters. Due to the current resolution of our images, we could not reliably measure the cooling length of the tail at 0.144 and 1.4 GHz—e.g., by fitting the surface brightness profile with an exponential model $I(r) \propto \exp(r/r_c)$—nor reliably detect it at 3.2 and 5.5 GHz. Therefore, we ultimately resolved to constrain the magnetic field by using the projected lengths observed at 0.144 and 1.4 GHz.

The $v_{\rm pl}$ is unknown, therefore we proposed two possible regimes:

1. Cloud velocity: the truncated radio disk, which has the same extension as the Hα emission, suggests that the relativistic plasma follows the same dynamics of the stripped ISM clouds, which have a characteristic velocity of $v_{\rm pl} = 100$–500 km s^{-1} (e.g., Tonnesen & Bryan 2021).
2. Postshock velocity: Müller et al. (2021) have suggested that the CRe move along the ordered magnetic field (re) accelerated by the bow shock. The actual velocity of JW100 is also unknown, but the estimate provided in Poggianti et al. (2019b; $\gtrsim$2200 km s^{-1}) entails a postshock velocity of $\sim$2000 km s^{-1}.

Currently, the lack of information about the polarization of the radio emission, hence also about the geometry of the magnetic field, does not allow us test the latter regime. Moreover, the spectral steepening observed in both the disk and the tail (Figure 5) might suggest that the role of shock reacceleration (i.e., spectral flattening at high frequencies) is negligible, hence that the contribution of the CRe moving at the postshock velocity might not be relevant. Therefore, on the basis of the morphological similarities between the Hα and the radio emission in the disk (which we further discuss in Section 4.2), we favor the first scenario.

This estimate has a series of caveats. To begin with, we are using the projected length of the tail, i.e., the lower limit of its actual extension, which is ultimately an observation-dependent quantity. Therefore, we can only estimate an upper limit for the magnetic field. Furthermore, we neglected any possible contributions to the CRe energy from turbulent reacceleration (e.g., Brunetti & Lazarian 2016) within the tail, which could extend their lifetimes, or any injections of fresh CRe from the SNe in the tail (i.e., we are assuming that the CRe are only accelerated within the disk). The former assumption could be supported by the fact that reacceleration has been claimed to be negligible for high-mass galaxies (Roberts et al. 2021b), whereas the latter could be viable if the radio emission of the stripped, relativistic plasma accelerated in the disk overcomes the nonthermal emission associated with the SFR in the tail. Keeping in mind these limitations, by assuming $v_{\rm pl} = 100$–500 km s^{-1}, we can match the projected tail lengths observed at 0.144 and 1.4 GHz, which are 37 and 21 kpc, respectively, for $B \leqslant 10$ μG, as shown in Figure 7.

Interestingly, we note that, within this framework, by assuming (a) a uniform magnetic field, and (b) that CRe with different energies travel along the tail at the same velocity, the cooling length should change with frequency as:

$$\frac{D_1}{D_2} = \frac{t_{\rm r,1}}{t_{\rm r,2}} \simeq \sqrt{\frac{\nu_2}{\nu_1}}. \quad (6)$$

The current observations do not resolve enough of the tail of JW100 to test this, thus we refer to deeper high-resolution observations of asymmetrical radio tails. Confirming (or not) the predictions of Equation (6) would permit is to probe the CRe dynamics within the tail of jellyfish galaxies.

4. Discussion

The multifrequency study presented in this work allows us to infer the characteristics of the nonthermal radio emission of JW100, providing us with important insights into the properties of the CRe and the magnetic field. In the following, we use these new pieces of information, together with the results of previous studies of this galaxy, to investigate a series of crucial questions—i.e., what is the origin of the CRe, what role does RPS play in their evolution, and what can we learn about the evolution of this peculiar galaxy thanks to the properties of its nonthermal components?

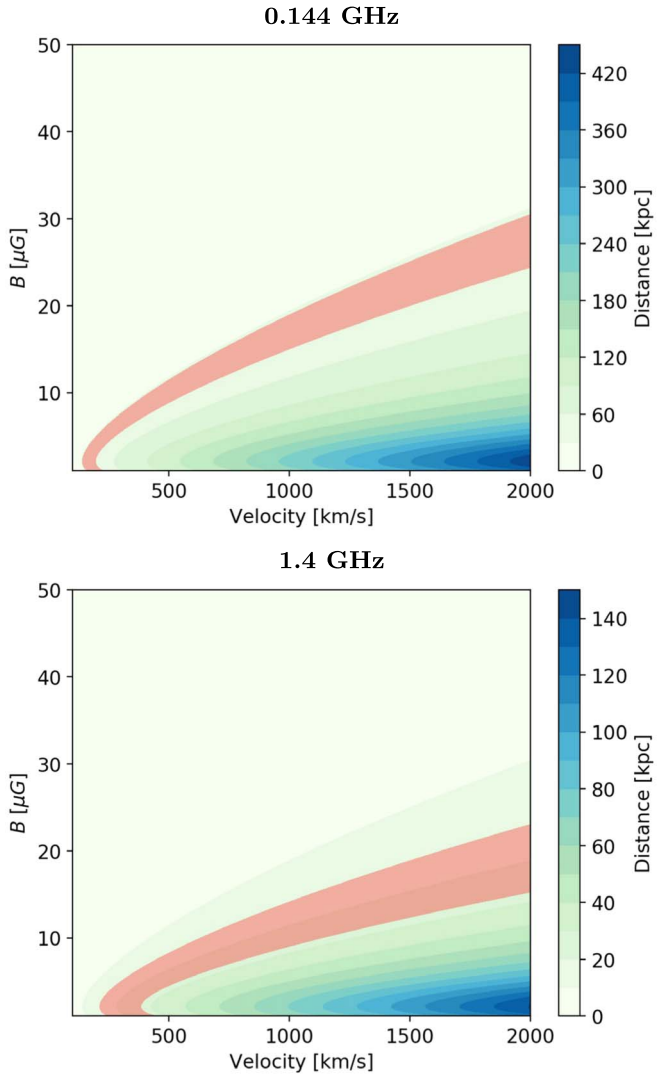

Figure 7. Cooling length parameter spaces for the radio tail observed at 0.144 (top) and 1.4 GHz (bottom). The red regions correspond to the observed projected lengths, which are here reported with a 6 kpc uncertainty due to the current resolution of 12″.

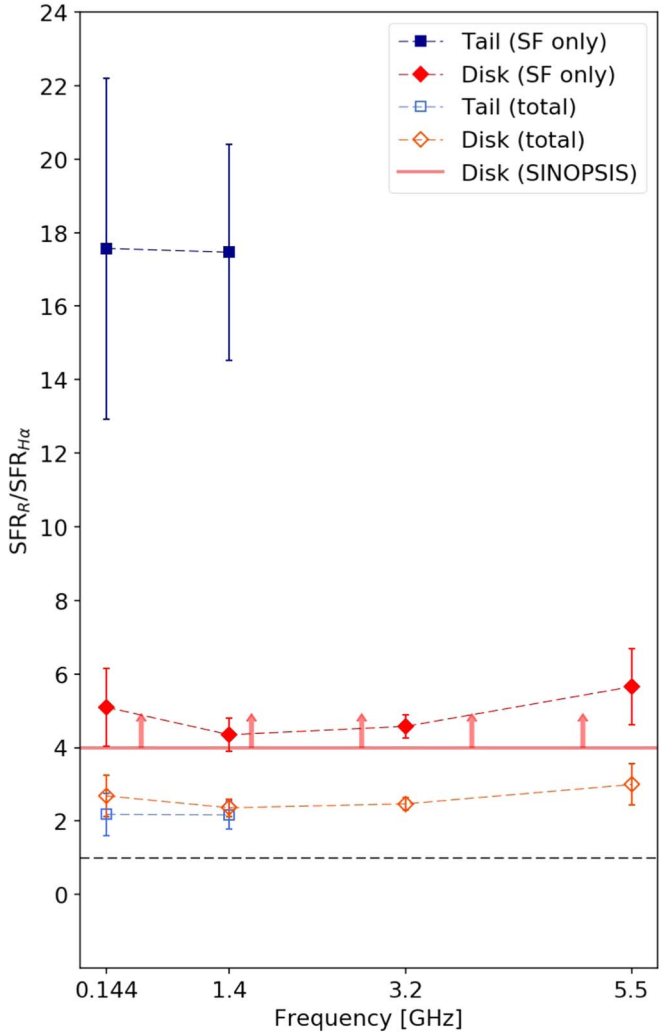

Figure 8. Ratio between SFR_R and $SFR_{H\alpha}$ for the disk (in red) and the tail (in blue) at the different frequencies. For reference, we also report the ratios computed by using the total Hα emission (the empty markers). The horizontal red line points out the median SFR ratio within the stellar disk derived from the SINOPSIS analysis (which is actually a lower limit; see Section 4.1), while the black dashed line indicates the level at which $SFR_R/SFR_{H\alpha} = 1$.

4.1. Origin and Evolution of the Radio-emitting Electrons

In this section, we investigate the origin of the CRe by exploring their connection with the star formation history of the galaxy. Both radio and Hα fluxes are SFR diagnostics (see, e.g., Kennicutt & Evans (2012) for a review), thus they can be used to compare the expected SFR in the disk and the tail. We estimated the radio-based SFR, SFR_R, at each frequency by adopting the conversion presented in Garn et al. (2009):

$$\mathrm{SFR_R} = \frac{0.066}{1+z}\left(\frac{D_L(z)}{\mathrm{Mpc}}\right)^2\left[\frac{(1+z)\nu}{1.4\ \mathrm{GHz}}\right]^{-\alpha_\nu^{1.4}}\left(\frac{S_{\mathrm{nt}}}{\mathrm{Jy}}\right) M_\odot\ \mathrm{yr}^{-1}, \quad (7)$$

where $D_L(z)$ is the luminosity distance at the redshift z, ν is the frequency, and $\alpha_\nu^{1.4}$ is the spectral index between ν and 1.4 GHz. This relation is an extension of the relation presented in Bell et al. (2003), and it is based on the Chabrier (2003) IMF. For the Hα-based estimate, $SFR_{H\alpha}$, we have adopted the conversion presented in Kennicutt (1998), converted to the Chabrier (2003) IMF accordingly:

$$\mathrm{SFR}_{H\alpha} = 4.6 \times 10^{-42}\left(\frac{L_{H\alpha}}{\mathrm{erg\ s^{-1}}}\right) M_\odot\ \mathrm{yr}^{-1}, \quad (8)$$

where $L_{H\alpha}$ is the Hα luminosity. We evaluated the SFR by using the respective fluxes measured from the images with a matching resolution of 12″ and, in the case of the Hα, we selected only those regions classified as star-forming according to the [O I] BPT diagrams. For reference, the SFR ratios were also evaluated by using the total Hα emission (see Figure 1), smoothed to 12″ × 12″ accordingly. The results are presented in Figure 8.

We found that, in the disk, the SFR estimated from the radio is 5 times larger than the SFR estimated from the Hα emission. In the tail, this discrepancy is even larger—a factor of 18. A similar discrepancy between the radio and Hα signals between disks and tails has also been observed in the galaxies in the Coma cluster (Chen et al. 2020; Figure 6). When the total Hα emission is included, the excesses decrease to a factor × 2.5 for

both the disk and the tail. Nevertheless, the excess of the radio emission with respect to the observed Hα emission persists.

The excess in the tail could be explained as further evidence that the relativistic plasma we observe in that region has been stripped from the disk, thus it is not related to the local star formation traced by the Hα emission. The discrepancy in the disk could instead be interpreted as evidence of a higher SFR in the past or, in other words, of recent quenching in the galaxy. Indeed, the total radio emission can trace the average SFR within the typical radiative time of the CRe (i.e., a few 10^7 yr), whereas the Hα emission traces the most recent phase ($<10^7$ yr) of star formation.

In order to test this scenario, we estimated the SFR in two different epochs by using the Simulating Optical Spectra with Stellar Population Models (SINOPSIS) analysis (Fritz et al. 2017). SINOPSIS is a spectrophotometric code that searches combinations of Single Stellar Population (SSP) model spectra to find the best fits with the equivalent widths of the main lines in absorption and emission and the continuum at various wavelengths, minimizing $\chi = 1$ by using an adaptive simulated annealing algorithm (Fritz et al. 2007, 2011). The star formation history is left free, with no analytic priors. SINOPSIS uses a Chabrier (2003) IMF with stellar masses in the 0.1–100 $M_\odot$ limits, and covers metallicity values from $Z = 0.0001$ to 0.04. The metallicity of the best-fit models is constant and homogeneous (i.e., all of the SSPs have the same metallicity, independent of age). The best-fit models are searched using SSP models at three different metallicity values (subsolar, solar, and supersolar). Dust extinction is accounted for by adopting the Galaxy extinction curve (Cardelli et al. 1989). SINOPSIS uses the latest SSP models from S. Charlot & G. Bruzual (2021, in preparation), based on stellar evolutionary tracks from Bressan et al. (2012) and stellar atmosphere spectra from a compilation of different authors, depending on the wavelength range, stellar luminosity, and effective temperature. SINOPSIS also includes the nebular emission lines for young SSPs (i.e., with ages $<2 \times 10^7$ yr), computed with the Cloudy code (Ferland et al. 2013). Among other quantities, the code provides, for each MUSE spaxel, the average SFR in twelve age bins. These bins can be combined into larger bins in such a way that the differences between the spectral characteristics of the stellar populations are maximal (Fritz et al. 2017). For the aim of our analysis, we estimated the time-averaged SFR within two intervals, $<5.7 \times 10^7$ ($\mathrm{SFR_{old}}$) and $<2 \times 10^6$ yr ($\mathrm{SFR_{young}}$), which roughly correspond to the timescales traced by the radio and Hα emissions, and we computed the pixel-by-pixel ratio between them in the star-forming spaxels (Figure 4), which we report in Figure 9.

Our analysis revealed that the SFR in the disk was generally higher in the past ($\mathrm{SFR_{old}/SFR_{young}} > 1$). Specifically, in the star-forming regions within the stellar disk, we measure a median value of 4, which is close to the radio excess observed in the same regions of the disk (Figure 8). We note that this value represents a lower limit for the actual ratio. Due to our selection of the star-forming regions, we are neglecting the past SFR of a large portion of the disk that has stopped forming stars only recently, hence it is not traced by the Hα emission. Moreover, by using the [O I] classification, we are more conservative in our selection of the star-forming regions than by using other BPT diagrams. We also note the time intervals we are considering are relatively young, and therefore prone to

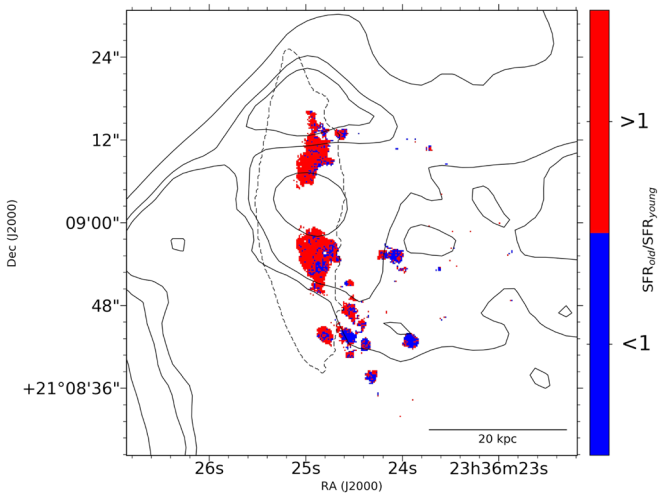

Figure 9. Ratio between the SFR within 5.7×10^7 and 2×10^6 yr, derived using SINOPSIS. We report the values lower than 1 in blue, and those above 1 in red. For reference, we also report the contours of the 0.144 GHz radio emission shown in Figure 2 (the continuous lines) and the stellar continuum (the dashed line).

degeneracies in age and dust attenuation in the SINOPSIS analysis.

On the basis of our findings, we suggest that the radio emission in the disk is actually dominated by a radiatively "old" plasma with a radiative age of a few 10^7 yr. Therefore, the spectral steepening observed in the disk is the result of the combination of the radio emissions produced by the old, steep-spectrum plasma accelerated during the past star-forming phase and the young, flat-spectrum plasma related to the ongoing star formation. Accordingly, the steeper spectrum we observe in the tail could be the consequence of a combination of two effects. On the one hand, the radio plasma naturally loses its energy while it travels to the tail, thus resulting in a steeper-spectrum radio emission (e.g., for a stripping velocity of 100–500 km $\mathrm{s^{-1}}$, the time required to cover 10 kpc would be of the order of a few 10^7 yr, which corresponds to the radiative time of the CRe emitting at GHz frequencies). On the other hand, by moving in a region with a lower magnetic field ($<10\ \mu$G; see Section 3.4), the CRe emit at lower frequencies, and thus the nonthermal spectrum gets shifted to lower frequencies (i.e., these observations sampled the steeper part of the spectrum). We also note that the SINOPSIS analysis revealed that the blobs outside the disk were dominated by the more recent star formation (i.e., the ratio between the SFR within 5.7×10^7 and 2×10^6 yr is lower than 1 in Figure 9). This indicates that these star-forming blobs are recent ($<2 \times 10^6$ yr), and hence that the stripped ISM can survive, cool down, and also form new stars outside the disk (see Vulcani et al. 2018; Poggianti et al. 2019b; Moretti et al. 2020a). As we discuss in Section 4.2, the local magnetic field can play a role in this by protecting the cold ISM from the hot, hostile ICM.

On the basis of the SINOPSIS analysis, we propose that the radio excess in the disk could be explained by a fast quenching of the galaxy, with the SFR decreasing by a factor 4 within the last few 10^7 yr. A similar scenario of star formation quenching —or lower star formation efficiency—within the disk of JW100 has also been proposed in Moretti et al. (2020a). They observed that the regions characterized by lower star formation efficiency were located at the center, in the proximity of the galactic bulge. The presence of a stellar bulge, as well as RPS, has been

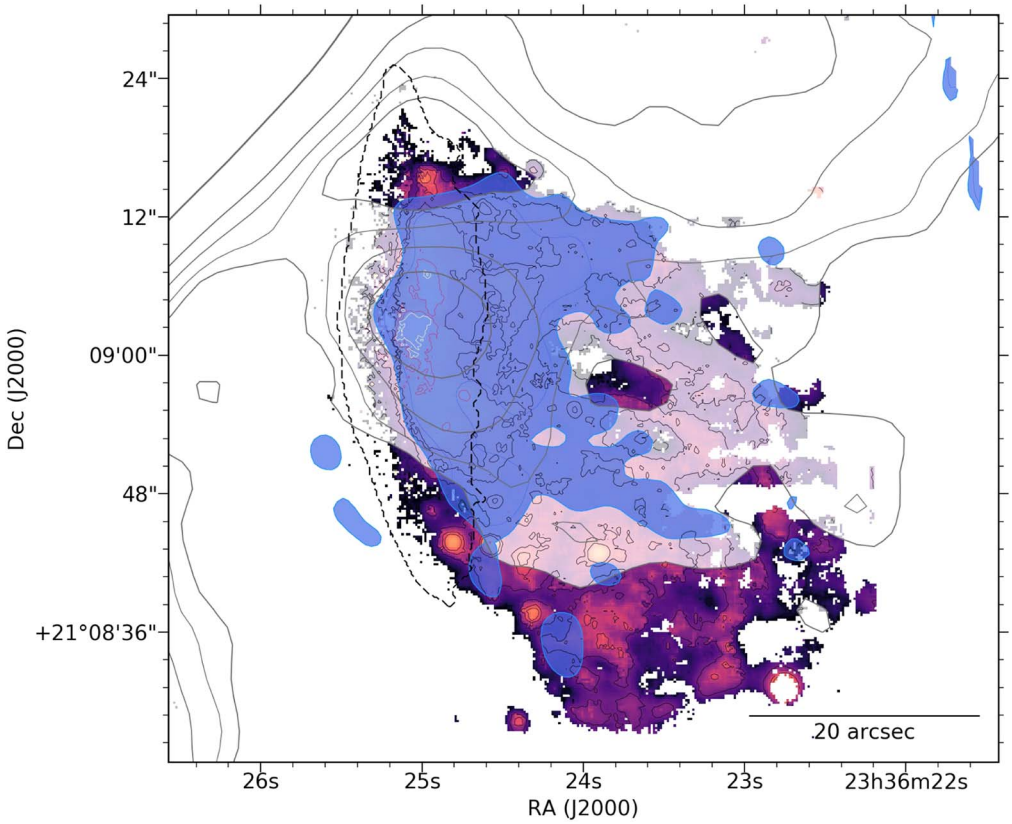

Figure 10. Multiwavelength image of JW100: the MUSE stellar continuum (the dashed black line) and Hα (the color map; 0.″2 resolution) with the contours of the 0.144 GHz emission from Figure 2 (the white-filled gray contours) and the Chandra X-ray image in 0.5–2.0 keV smoothed with a 1.″5 Gaussian (the blue-filled areas).

observed to be systematically able to suppress the SFR (e.g., Gensior et al. 2020), hence we suggest that the SFR_R–$SFR_{H\alpha}$ discrepancy could be the natural outcome of this.

However, we cannot exclude the possibility that the radio excess could also depend on other factors. The compression of the ISM—i.e., of the magnetic field—by the ram pressure would result in the enhancement of the radio emission (e.g., Markevitch et al. 2005), and thus in a higher estimate of SFR_R. This scenario was proposed to explain the general excess of radio emission observed in cluster late-type galaxies (e.g., Gavazzi & Boselli 1999). Another possible source of additional radio emission could be the acceleration of galactic CRe as result of interactions with the ICM winds (Murphy et al. 2009) or an additional component of radio emission associated with the magnetized drape. Alternatively, due to the low resolution, we cannot completely exclude the possibility that there is a contribution of the AGN radio emission in the disk region.

4.2. Insights into the ISM–ICM Interplay

By combining radio, Hα, and X-ray images of JW100 (Figure 10), we can explore the connection between the different ISM components, namely the relativistic plasma, the warm ISM, and the hot galactic plasma likely produced by the interplay between ISM and ICM (e.g., Sun et al. 2010, 2021; Poggianti et al. 2019b; Campitiello et al. 2021). We observe that disk truncation is a common characteristic of radio, Hα, and X-ray emissions, thus hinting that (1) ram pressure stripping is equally relevant for the three corresponding components, or (2) both the radio and the X-ray extraplanar emissions are somehow a consequence of the warm ISM being stripped. The first hypothesis could be consistent with a scenario in which the relativistic plasma is stripped along the ISM clouds (e.g., in form of the magnetic field and CRe traveling within the stripped ISM clouds). The second hypothesis, instead, may be related to ICM draping (Dursi & Pfrommer 2008; Pfrommer & Dursi 2010). According to the draping scenario, the magnetized layer is composed of hot ICM. As a consequence of the density fluctuations induced by the passage of the bow shock, the magnetized layer can cool down, resulting in an extended X-ray emission (Sparre et al. 2020). Therefore, spatial correlation between the radio and X-ray emissions would be expected, because these emissions are produced within the same hot, magnetized layer. Interestingly, the lack of flat-spectrum emission outside the star-forming regions may suggest that the CRe (re)accelerated by the bow shock marginally contribute to the radio emission, thus questioning to what degree the bow shock may have actually affected the CRe. We refer to future polarimetric studies, which are beyond the scope of the present work, to further test this scenario by probing the presence of the signature ordered field (i.e., a high degree of extended polarized emission aligned along the tail) produced by the ICM draping.

Outside the disk, the spatial correlation between these phases seems to decrease, in the sense that the radio and X-ray emission seem to elongate mostly toward the west,[16] whereas the Hα emission is more extended toward the southwest. The discrepancy between the different emissions could be due to

[16] Even though the 0.144 GHz radio emission seems to be more extended toward the west than the Hα, we note that this is likely due to the different resolutions and the fact that the western edge of the radio tail falls outside the MUSE CCD.

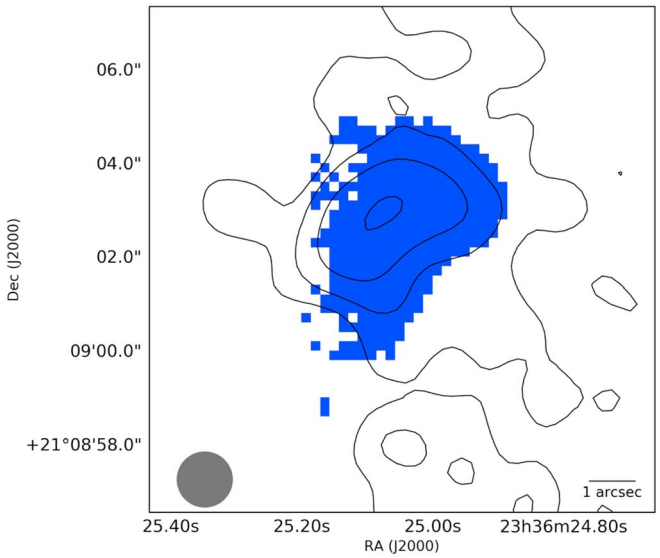

Figure 11. A zoom into the AGN region selected according to [O I] classification (Poggianti et al. 2019a), with the 3, 6, 12, and 24 σ contours from the VLA observations at 1.4 GHz presented in Gitti (2013; $1\farcs3 \times 1\farcs3$ resolution, as reported in the bottom-left corner, and $1\sigma = 12.9$ μJy beam^{-1}).

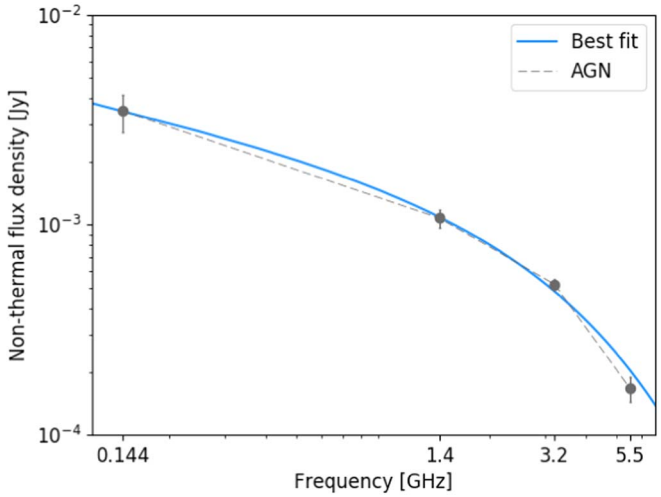

Figure 12. AGN nonthermal spectrum from Figure 5 and the best-fitting exponential cut-off model.

sensitivity issues or the different timescales of the emissions. Specifically, the lack of radio emission in the southern part of the tail could indicate that this region is a few radiative times older than the 0.144 GHz emission (i.e., a few 10^8 yr), thus without the injection of fresh CRe, the radio emission is no longer visible in our images. Noticeably, the lack of X-ray emission in the farthest part of the tail might suggest that the interaction between ISM and ICM there, and the cooling of the latter, is dominated by mixing instead of shock-induced radiative cooling (e.g., Gronke & Oh 2018; Kanjilal et al. 2020). However, investigating the physics of mixing is extremely complex, and beyond the scope of this work. Interestingly, the magnetic field tentatively constrained by the cooling length ($\leqslant 10$ μG; see Section 3.4) would potentially be strong enough to preserve the stripped ISM from the interactions with the ICM, in the form of conduction or hydrodynamical instabilities (e.g., Berlok & Pfrommer 2019; Cottle et al. 2020), thus allowing the stripped clouds to survive outside the disk and, potentially, form new stars (e.g., Sparre et al. 2020; Ge et al. 2021).

4.3. On the AGN Radio Emission

JW100 hosts a central AGN (Seyfert2), with evidence of optical (Poggianti et al. 2019a, 2019b) radio (Gitti 2013; Ignesti et al. 2017) and X-ray (Wong et al. 2008; Poggianti et al. 2019b) emissions. The AGN is also characterized by the presence of an ionized gas outflow (Radovich et al. 2019). In agreement with the high-resolution images presented in Gitti (2013) and Ignesti et al. (2017), we detect a peak in surface brightness coinciding with its position. Interestingly, Figure 11 shows that that the morphology of the radio emission derived from the high-resolution VLA image of A2626 presented in Gitti (2013) coincides remarkably well with the optical emission due to the AGN, traced by the [O I] BPT diagram (Poggianti et al. 2019b). Kiloparsec-scale radio emission in Seyfert galaxies is common (Gallimore et al. 2006), and it is explained by the "frustrated jet model." This scenario predicts that the kinetic energy of the relativistic jets can be transferred to the ISM, possibly triggering a gas outflow from the inner region of the galaxy (we refer to Bicknell et al. (1997) for a more detailed formulation). Taking into account the caveats reported in Section 3.2, the AGN nonthermal spectrum allows us to tentatively explore the connection between the origin of the radio emission and the ionized gas outflow observed in JW100.

Our new multifrequency analysis revealed that the AGN is characterized by a steep spectrum above 1.4 GHz (Figure 5) that could be an indication of a radiatively old relativistic plasma. We tested this hypothesis by fitting the observed nonthermal spectrum with an exponential cut-off model, which is suited to fit the exponential decline produced by energy losses (e.g., Eilek & Arendt 1996):

$$S(\nu) \propto \nu^{\alpha} e^{-\frac{\nu}{\nu_b}}. \quad (9)$$

By fitting the observed spectrum, we estimate a break frequency of $\nu_b = 3.4 \pm 0.8$ GHz (Figure 12). For $B = 11$–18 μG, CRe emitting at this frequency have typical radiative ages of $(0.7\text{–}1.3) \times 10^7$ yr (Equation (5)), which is in agreement with the age of the ionized gas outflow estimated in Radovich et al. (2019; 0.8×10^7 yr). Therefore, we suggest that the ejection/acceleration of the radio plasma within the AGN region, possibly due to the presence of unresolved, frustrated radio jets, might be linked to the arcsec-scale ionized gas outflow observed by MUSE.

5. Summary and Conclusions

We have presented a detailed analysis of the radio emission of the jellyfish galaxy JW100, based on an unprecedented assembly of radio observations. By combining LOFAR, MeerKAT, and VLA observations, as well as using previous results obtained with MUSE and Chandra, we have investigated the properties and the origin of the radio-emitting relativistic plasma. We studied the spectrum of the star-forming regions within the disk, finding that below 1.4 GHz the nonthermal spectrum shows signatures of the results of several energy loss mechanisms, whereas at higher frequencies it shows the characteristic steepening ($\alpha = -2.40 \pm 0.36$ between 3.2 and 5.5 GHz) produced by an advanced radiative stage. By comparing our findings with the results of the

SINOPSIS analysis, we concluded that the nonthermal emission in the disk is dominated by the old CRe injected when the SFR was, at least, a factor $\times 4$ higher than that currently inferred from the Hα emission. We also estimated the magnetic field in the galaxy using different methods. We observed a decrease in the magnetic field from the disk (11–18 μG) to the tail ($\leqslant$10 μG). Interestingly, the magnetic field in the tail would be strong enough to extend the life of the stripped ISM in the ICM, by protecting the cold gas from thermal conduction and hydrodynamical instabilities. Finally, we investigated the synchrotron spectrum of the AGN, finding that its radiative age is in agreement with the age of the ionized gas outflow, thus suggesting a connection between the acceleration of the relativistic plasma and the gas outflow.

The study presented here offers a series of new insights into the physics of ram pressure stripping, provided by the nonthermal radio emission. The observed spatial correlation between the radio and X-ray emission might suggest a physical connection between these phases, which would be in agreement with the ICM draping scenario. Moreover, our multiwavelength analysis has proved that the nonthermal radio emission can be a powerful tool for probing the star formation history of a galaxy. On the basis of the excess of radio emission with respect to the current star formation, we could confirm the fast quenching of JW100. We further argue that a similar scenario is likely to have taken place in the other high-mass jellyfish galaxies, thus the radio excess observed in ram pressure stripped galaxies could similarly be interpreted as the result of the fast quenching of the SFR.

More insights will come from future high-resolution observations, such as LOFAR observations with a 0.″3 resolution performed with the international stations, and the studies to be carried out with the upcoming Square Kilometer Array, which will allow for a more detailed comparison of the optical and X-ray observations. Furthermore, deep observations designed for polarimetric studies at higher frequencies are now crucial for addressing the open questions about the geometry of the magnetic field posed by the present work.

We thank the anonymous referee for their thoughtful work that improved the presentation of the manuscript. A.I. thanks I. Ruffa for useful discussions. This work is the fruit of the collaboration between GASP and the LOFAR Survey Key Project team ("MoU: Exploring the low-frequency side of jellyfish galaxies with LOFAR"; PI: A. Ignesti, B. M. Poggianti, S. McGee). A.I., B.V., R.P., and M.G. acknowledge the Italian PRIN-Miur 2017 (PI: A. Cimatti). M.V. acknowledges support from the Netherlands Organisation for Scientific Research (NWO) through VICI grant 639.043.511. I.D.R. and R.J.v.W. acknowledge support from the ERC Starting Grant Cluster Web 804208. A.B. acknowledges support from the VIDI research program with project number 639.042.729, which is financed by the NWO. S.L.M. acknowledges support from the Science and Technology Facilities Council through grant No. ST/N021702/1. J.F. acknowledges financial support from the UNAM-DGAPA-PAPIIT IN111620 grant, Mexico. We acknowledge funding from the INAF mainstream funding program (PI: B. Vulcani), based on observations collected at the European Organization for Astronomical Research in the Southern Hemisphere under ESO program 196.B-0578. This project has received funding from the European Research Council (ERC) under the European Union's Horizon 2020 research and innovation program (grant agreement No. 833824). The LOFAR data products were provided by the LOFAR Surveys Key Science project (LSKSP; https://lofar-surveys.org/) and were derived from observations with the International LOFAR Telescope (ILT). LOFAR (van Haarlem et al. 2013) is the Low Frequency Array designed and constructed by ASTRON. It has observing, data processing, and data storage facilities in several countries, which are owned by various parties (each with their own funding sources), and which are collectively operated by the ILT foundation under a joint scientific policy. The efforts of the LSKSP have benefited from funding from the ERC, NOVA, NWO, CNRS-INSU, the SURF Co-operative, the UK Science and Technology Funding Council, and the Jülich Supercomputing Centre. This paper makes use of MeerKAT data (Project ID: SCI-20190418-JH-01). The MeerKAT telescope is operated by the South African Radio Astronomy Observatory, which is a facility of the National Research Foundation, an agency of the Department of Science and Innovation. A.I. thanks the music of Black Sabbath for providing inspiration during the preparation of the draft.

ORCID iDs

Alessandro Ignesti https://orcid.org/0000-0003-1581-0092
Benedetta Vulcani https://orcid.org/0000-0003-0980-1499
Bianca M. Poggianti https://orcid.org/0000-0001-8751-8360
Rosita Paladino https://orcid.org/0000-0001-9143-6026
Timothy Shimwell https://orcid.org/0000-0001-5648-9069
Julia Healy https://orcid.org/0000-0003-1020-8684
Myriam Gitti https://orcid.org/0000-0002-0843-3009
Cecilia Bacchini https://orcid.org/0000-0002-8372-3428
Alessia Moretti https://orcid.org/0000-0002-1688-482X
Mario Radovich https://orcid.org/0000-0002-3585-866X
Reinout J. van Weeren https://orcid.org/0000-0002-0587-1660
Ian D. Roberts https://orcid.org/0000-0002-0692-0911
Andrea Botteon https://orcid.org/0000-0002-9325-1567
Ancla Müller https://orcid.org/0000-0001-9184-7845
Sean McGee https://orcid.org/0000-0003-3255-3139
Jacopo Fritz https://orcid.org/0000-0002-7042-1965
Neven Tomičić https://orcid.org/0000-0002-8238-9210
Ariel Werle https://orcid.org/0000-0002-4382-8081
Matilde Mingozzi https://orcid.org/0000-0003-2589-762X
Marco Gullieuszik https://orcid.org/0000-0002-7296-9780
Marc Verheijen https://orcid.org/0000-0001-9022-8081

References

Bacchini, C., Fraternali, F., Iorio, G., et al. 2020, A&A, 641, A70
Basu, A., Beck, R., Schmidt, P., & Roy, S. 2015, MNRAS, 449, 3879
Beck, R. 2000, RSPTA, 358, 777
Beck, R., & Krause, M. 2005, AN, 326, 414
Bell, E. F., McIntosh, D. H., Katz, N., & Weinberg, M. D. 2003, ApJS, 149, 289
Berlok, T., & Pfrommer, C. 2019, MNRAS, 489, 3368
Bicknell, G. V., Dopita, M. A., & O'Dea, C. P. O. 1997, ApJ, 485, 112
Boselli, A., Fossati, M., & Sun, M. 2021, arXiv:2109.13614
Boselli, A., & Gavazzi, G. 2006, PASP, 118, 517
Bressan, A., Marigo, P., Girardi, L., et al. 2012, MNRAS, 427, 127
Briggs, D. S. 1995, BAAS, 27, 1444
Brunetti, G., & Lazarian, A. 2016, MNRAS, 458, 2584
Campitiello, M. G., Ignesti, A., Gitti, M., et al. 2021, ApJ, 911, 144
Cardelli, J. A., Clayton, G. C., & Mathis, J. S. 1989, ApJ, 345, 245
Cava, A., Bettoni, D., Poggianti, B. M., et al. 2009, A&A, 495, 707
Chabrier, G. 2003, PASP, 115, 763

Chen, H., Sun, M., Yagi, M., et al. 2020, MNRAS, 496, 4654
Chyży, K. T., Jurusik, W., Piotrowska, J., et al. 2018, A&A, 619, A36
Condon, J. J. 1992, ARA&A, 30, 575
Cottle, J., Scannapieco, E., Brüggen, M., Banda-Barragán, W., & Federrath, C. 2020, ApJ, 892, 59
Deeg, H. J., Duric, N., & Brinks, E. 1997, A&A, 323, 323
Dursi, L. J., & Pfrommer, C. 2008, ApJ, 677, 993
Ebeling, H., Ma, C.-J., & Barrett, E. 2014, ApJS, 211, 21
Eilek, J. A., & Arendt, P. N. 1996, ApJ, 457, 150
Ferland, G. J., Porter, R. L., van Hoof, P. A. M., et al. 2013, RMxAA, 49, 137
Fritz, J., Moretti, A., Gullieuszik, M., et al. 2017, ApJ, 848, 132
Fritz, J., Poggianti, B. M., Bettoni, D., et al. 2007, A&A, 470, 137
Fritz, J., Poggianti, B. M., Cava, A., et al. 2011, A&A, 526, A45
Fumagalli, M., Fossati, M., Hau, G. K. T., et al. 2014, MNRAS, 445, 4335
Gallimore, J. F., Axon, D. J., O'Dea, C. P., & Baum, S. A. 2006, AJ, 132, 546
Garn, T., Green, D. A., Riley, J. M., & Alexander, P. 2009, MNRAS, 397, 1101
Gavazzi, G., & Boselli, A. 1999, A&A, 343, 93
Gavazzi, G., Boselli, A., Cortese, L., et al. 2006, A&A, 446, 839
Ge, C., Luo, R., Sun, M., et al. 2021, MNRAS, 505, 4702
Gensior, J., Kruijssen, J. M. D., & Keller, B. W. 2020, MNRAS, 495, 199
Gitti, M. 2013, MNRAS, 436, L84
Govoni, F., & Feretti, L. 2004, IJMPD, 13, 1549
Gressel, O., Elstner, D., Ziegler, U., & Rüdiger, G. 2008, A&A, 486, L35
Gronke, M., & Oh, S. P. 2018, MNRAS, 480, L111
Gronke, M., & Oh, S. P. 2020, MNRAS, 492, 1970
Guglielmo, V., Poggianti, B. M., Moretti, A., et al. 2015, MNRAS, 450, 2749
Gullieuszik, M., Poggianti, B. M., McGee, S. L., et al. 2020, ApJ, 899, 13
Gunn, J. E., & Gott, J. R., III 1972, ApJ, 176, 1
Gürkan, G., Hardcastle, M. J., Smith, D. J. B., et al. 2018, MNRAS, 475, 3010
Healy, J., Deb, T., Verheijen, M. A. W., et al. 2021, A&A, 654, A173
Heesen, V., Buie, E., & Huff, I. 2019, A&A, 622, A8
Heesen, V., Dettmar, R.-J., Krause, M., Beck, R., & Stein, Y. 2016, MNRAS, 458, 332
Iapichino, L., & Brüggen, M. 2012, MNRAS, 423, 2781
Ignesti, A., Gitti, M., Brunetti, G., Feretti, L., & Giovannini, G. 2017, A&A, 604, A21
Ignesti, A., Gitti, M., Brunetti, G., et al. 2018, A&A, 610, A89
Ignesti, A., Shimwell, T., Brunetti, G., et al. 2020, A&A, 643, A172
Józsa, G. I. G., White, S. V., Thorat, K., et al. 2020, CARACal: Containerized Automated Radio Astronomy Calibration Pipeline, Astrophysics Source Code Library, ascl:2006.014
Kanjilal, V., Dutta, A., & Sharma, P. 2020, MNRAS, 501, 1143
Kennicutt, R. C., Calzetti, D., Aniano, G., et al. 2011, PASP, 123, 1347
Kennicutt, R. C., & Evans, N. J. 2012, ARA&A, 50, 531
Kennicutt, R. C., Jr. 1989, ApJ, 344, 685
Kennicutt, R. C., Jr. 1998, ARA&A, 36, 189
Klein, U., Lisenfeld, U., & Verley, S. 2018, A&A, 611, A55
Krause, M., Irwin, J., Wiegert, T., et al. 2018, A&A, 611, A72
Markevitch, M., Govoni, F., Brunetti, G., & Jerius, D. 2005, ApJ, 627, 733
McMullin, J. P., Waters, B., Schiebel, D., Young, W., & Golap, K. 2007, in ASP Conf. Ser. 376, Astronomical Data Analysis Software and Systems XVI, ed. R. A. Shaw, F. Hill, & D. J. Bell (San Francisco, CA: ASP), 127
Miley, G. 1980, ARA&A, 18, 165
Moretti, A., Paladino, R., Poggianti, B. M., et al. 2020a, ApJ, 889, 9
Moretti, A., Paladino, R., Poggianti, B. M., et al. 2020b, ApJL, 897, L30
Moretti, A., Poggianti, B. M., Gullieuszik, M., et al. 2018, MNRAS, 475, 4055
Müller, A., Poggianti, B. M., Pfrommer, C., et al. 2021, NatAs, 5, 159
Murphy, E. J. 2009, ApJ, 706, 482
Murphy, E. J., Condon, J. J., Schinnerer, E., et al. 2011, ApJ, 737, 67
Murphy, E. J., Kenney, J. D. P., Helou, G., Chung, A., & Howell, J. H. 2009, ApJ, 694, 1435
Offringa, A. R., McKinley, B., Hurley-Walker, N., et al. 2014, MNRAS, 444, 606
Offringa, A. R., & Smirnov, O. 2017, MNRAS, 471, 301
Pacholczyk, A. G. (ed.) 1970, Radio Astrophysics. Nonthermal Processes in Galactic and Extragalactic Sources (San Francisco, CA: Freeman)
Peluso, G., Vulcani, B., & Poggianti, B. M. 2021, arXiv:2111.02538
Pfrommer, C., & Dursi, L. J. 2010, NatPh, 6, 520
Poggianti, B. M., Fasano, G., Omizzolo, A., et al. 2016, AJ, 151, 78
Poggianti, B. M., Gullieuszik, M., Tonnesen, S., et al. 2019a, MNRAS, 482, 4466
Poggianti, B. M., Ignesti, A., Gitti, M., et al. 2019b, ApJ, 887, 155
Poggianti, B. M., Jaffé, Y. L., Moretti, A., et al. 2017a, Natur, 548, 304
Poggianti, B. M., Moretti, A., Gullieuszik, M., et al. 2017b, ApJ, 844, 48
Radovich, M., Poggianti, B., Jaffé, Y. L., et al. 2019, MNRAS, 486, 486
Roberts, I. D., van Weeren, R. J., McGee, S. L., et al. 2021a, A&A, 652, A153
Roberts, I. D., van Weeren, R. J., McGee, S. L., et al. 2021b, A&A, 650, A111
Sarazin, C. L. 1986, RvMP, 58, 1
Schleicher, D. R. G., & Beck, R. 2013, A&A, 556, A142
Serra, P., Maccagni, F. M., Kleiner, D., et al. 2019, A&A, 628, A122
Shimwell, T. W., Röttgering, H. J. A., Best, P. N., et al. 2017, A&A, 598, A104
Shimwell, T. W., Tasse, C., Hardcastle, M. J., et al. 2019, A&A, 622, A1
Smith, R. J., Lucey, J. R., Hammer, D., et al. 2010, MNRAS, 408, 1417
Sparre, M., Pfrommer, C., & Ehlert, K. 2020, MNRAS, 499, 4261
Sun, M., Donahue, M., Roediger, E., et al. 2010, ApJ, 708, 946
Sun, M., Ge, C., Luo, R., et al. 2021, NatAs, in press
Tabatabaei, F. S., Schinnerer, E., Krause, M., et al. 2017, ApJ, 836, 185
Tonnesen, S., & Bryan, G. L. 2021, ApJ, 911, 68
van Gorkom, J. H. 2004, in Clusters of Galaxies: Probes of Cosmological Structure and Galaxy Evolution, ed. J. S. Mulchaey, A. Dressler, & A. Oemler (Cambridge: Cambridge Univ. Press), 305
van Haarlem, M. P., Wise, M. W., Gunst, A. W., et al. 2013, A&A, 556, A2
van Weeren, R. J., Shimwell, T. W., Botteon, A., et al. 2021, A&A, 651, A115
Vollmer, B., Beck, R., Kenney, J. D. P., & van Gorkom, J. H. 2004, AJ, 127, 3375
Vollmer, B., Soida, M., Beck, R., et al. 2013, A&A, 553, A116
Vollmer, B., Soida, M., Chung, A., et al. 2009, A&A, 496, 669
Vulcani, B., Poggianti, B. M., Gullieuszik, M., et al. 2018, ApJL, 866, L25
Wong, K.-W., Sarazin, C. L., Blanton, E. L., & Reiprich, T. H. 2008, ApJ, 682, 155
Zhang, Y., Yang, X., Wang, H., et al. 2013, ApJ, 779, 160